

# Demonstration of the broadband half-wave plate using the nine-layer sapphire for the CMB polarization experiment

Kunimoto Komatsu<sup>a</sup>, Tomotake Matsumura<sup>b</sup>, Hiroaki Imada<sup>c</sup>, Hirokazu Ishino<sup>a</sup>, Nobuhiko Katayama<sup>b</sup>, Yuki Sakurai<sup>b</sup>

<sup>a</sup>Okayama University, Okayama 700-8530, Japan

<sup>b</sup>Kavli Institute for the Physics and Mathematics of the Universe (WPI), University of Tokyo, Kashiwa 277-8583, Japan

<sup>c</sup>Laboratoire de l'Accélérateur Linéaire, Université Paris-Sud, CNRS/IN2P3, Université Paris-Saclay, Orsay, France

**Abstract.** We report the development of the achromatic half-wave plate (AHWP) at millimeter wave for cosmic microwave background polarization experiments. We fabricate an AHWP consisting of nine a-cut sapphire plates based on the Pancharatnam recipe to cover a wide frequency range. The modulation efficiency and the phase are measured in a frequency range of 33 to 260 GHz with incident angles up to 10 degrees. We find the measurements at room temperature are in good agreement with the predictions. This is the broadest demonstration of the AHWP at the millimeter wave.

**Keywords:** CMB polarization, B-mode, Achromatic half-wave plate, Space mission, Polarimetry, Millimeter wave.

\*Kunimoto Komatsu, [k.komatsu@s.okayama-u.ac.jp](mailto:k.komatsu@s.okayama-u.ac.jp)

## 1 INTRODUCTION

Cosmic inflation is one of the theoretical models that give rise to the initial condition of the hot big-bang in our universe. The rapid space expansion, immediately after the beginning of the universe, produced quantum fluctuations in space-time. Thus, it generated primordial gravitational waves, which imprinted the B-mode polarization in the cosmic microwave background (CMB). The strength of the gravitational waves is represented by a tensor-to-scalar ratio  $r$ . The majority of the single-scalar-field slow-roll inflation models predict the value of  $r$  to be  $> 0.01$ . The target accuracy for future CMB polarization measurements is set to be less than 0.001.

The required level of the B-mode polarization measurements for the primordial gravitational waves is an order of nano-Kelvin; a precise control of systematic effects is needed. The main systematic source is caused by the different characteristics in a pair of detectors mutually orthogonal in the polarization sensitive orientation. The  $1/f$  noise in the measurement system also causes a big contamination in the large angular scales where the primordial gravitational wave signal is prominent. The measurements with a polarization modulation employing a rotating half-wave plate (HWP) can mitigate those systematics, however. On the other hand, more than 99% of the polarized foreground emission has to be subtracted to achieve the target precision of  $r$ . The standard way to differentiate the foreground emission and the CMB is to make use of the difference in frequency spectra of the sources; the CMB is known to have a perfect blackbody while the foreground emission, such as the synchrotron and dust emissions, have spectra different from the CMB. In order to measure the difference of the spectrum shape, we need an optical system covering broad frequency coverage.

In the past, the HWP was first implemented to the CMB experiment by MAXIPOL,<sup>1</sup> and has been followed by a number of CMB experiments, including ABS, EBEX, SPIDER, POLAR-BEAR.<sup>2-5</sup> Upcoming experiments also plan to employ a similar system.<sup>6-9</sup> The HWP is made of a birefringent material plate with an optic axis parallel to the surface. When the thickness of

the plate is chosen properly, the phase difference between the ordinary and extraordinary electric waves passing through the plate becomes  $\pi$  radians, i.e., a half wavelength. When the HWP is rotated with respect to a linear polarization-sensitive detector (in Figure 1), the incident plane of polarization rotates at a rate of twice the HWP rotation angle, and the measured intensity by the detector appears at a rate of four times the HWP angle. The continuously rotating HWPs modulate the signal at four times the rotational frequency of the HWP. As a result, we can reconstruct linear polarization components  $Q$  and  $U$  from the signal modulated at four times the rotational frequency of a HWP with a single detector. Correspondingly, the requirement to match the detector properties between two detectors is greatly relaxed.

The retardance of a waveplate can be written as  $\delta = 2\pi \frac{\Delta n d}{\lambda}$ , where  $\Delta n = |n_e - n_o|$  is the difference between the indices  $n_o$  and  $n_e$  for the ordinary and extraordinary rays, respectively,  $d$  is the thickness, and  $\lambda$  is the wavelength. The single HWP, which is made of a birefringent material plate, can be used only at the specific wavelength and its harmonics determined by the material and thickness. While the single HWP is generally a single-frequency device, Pancharatnam proposed to stack multiple wave plates to broaden the frequency range.<sup>10,11</sup>

In this paper, we describe our prototype design of the Pancharatnam-based achromatic HWP (AHWP) composed of nine sapphire plates for use in the CMB polarimetry. The design and the experimental demonstration appear in Hanany et al. (2005), Savini et al. (2006), and Pisano et al. (2006).<sup>12-14</sup> We designed and constructed the prototype AHWP and evaluated it experimentally in a millimeter wave band, from 33 to 260 GHz, which is the widest demonstrated bandwidth at millimeter-wave and possibly in all the optical wavelength. We discussed the results including all the features which we have observed in the measured modulation efficiency. This development is motivated to develop a broadband HWP for the next-generation CMB polarization satellite, LiteBIRD.<sup>15,16</sup>

## 2 FORMALISM

We construct the system in Figure 1, where the power of polarized light after passing through a continuous rotating AHWP is measured by a single polarization sensitive detector. The polarization state is expressed by using Stokes vectors and Mueller matrices as,

$$S_{\text{out}} = GR(-\omega_{\text{hwp}}t)\Gamma_{\text{AHWP}}R(\omega_{\text{hwp}}t)S_{\text{in}}, \quad (1)$$

$$R(\rho) = \begin{pmatrix} 1 & 0 & 0 & 0 \\ 0 & \cos 2\rho & -\sin 2\rho & 0 \\ 0 & \sin 2\rho & \cos 2\rho & 0 \\ 0 & 0 & 0 & 1 \end{pmatrix}, \quad (2)$$

$$G = \frac{1}{2} \begin{pmatrix} 1 & 1 & 0 & 0 \\ 1 & 1 & 0 & 0 \\ 0 & 0 & 0 & 0 \\ 0 & 0 & 0 & 0 \end{pmatrix}, \quad (3)$$

$$\Gamma_{\text{AHWP}} = \begin{pmatrix} M_{\text{II}} & M_{\text{IQ}} & M_{\text{IU}} & M_{\text{IV}} \\ M_{\text{QI}} & M_{\text{QQ}} & M_{\text{QU}} & M_{\text{QV}} \\ M_{\text{UI}} & M_{\text{UQ}} & M_{\text{UU}} & M_{\text{UV}} \\ M_{\text{VI}} & M_{\text{VQ}} & M_{\text{VU}} & M_{\text{VV}} \end{pmatrix}, \quad (4)$$

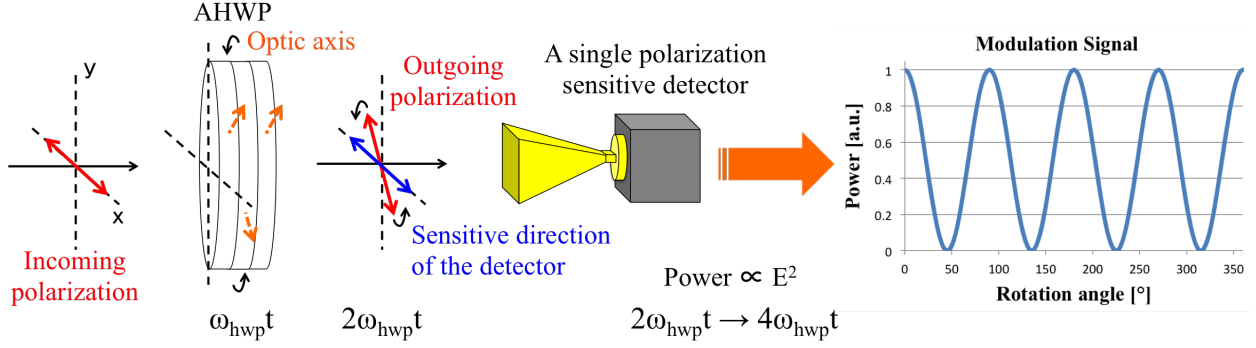


**Fig 1** A conceptual sketch of the three-layer AHWP polarimetry. The linearly polarized plane waves propagate from left to right in this figure. An example of the modulated signal resulting from one revolution of the HWP is shown in the most right hand side. The amplitude is related to the polarized intensity and the phase is related to the polarization angle of the incident radiation.

where  $S_{\text{in}} = (I_{\text{in}}, Q_{\text{in}}, U_{\text{in}}, V_{\text{in}})$  and  $S_{\text{out}} = (I_{\text{out}}, Q_{\text{out}}, U_{\text{out}}, V_{\text{out}})$  are the Stokes vectors of the incident and outgoing radiation.  $\Gamma_{\text{AHWP}}$  is the Mueller matrix of an AHWP,  $R$  is the rotation matrix,  $\rho$  is the rotation angle of the AHWP with respect to the detector coordinate,  $G$  is Mueller matrix for a polarizer which defines the polarization-sensitive orientation of the detector,  $t$  is time, and  $\omega_{\text{hwp}}$  is the angular frequency of the AHWP rotation.

In this paper, we set  $V_{\text{in}} = 0$  because the CMB is expected to be linearly polarized. For the normal incidence, the detected signal,  $I_{\text{out}}$ , can be written as a function of time as:

$$\begin{aligned}
 I_{\text{out}}(t) = & D_{0I}I_{\text{in}} + D_{0Q}Q_{\text{in}} + D_{0U}U_{\text{in}} \\
 & + D_{2I}I_{\text{in}} \cos(2\omega_{\text{hwp}}t - 2\phi_0) + D_2 \sqrt{Q_{\text{in}}^2 + U_{\text{in}}^2} \cos(2\omega_{\text{hwp}}t - 2\phi_2 - \arctan \frac{U_{\text{in}}}{Q_{\text{in}}}) \\
 & + D_4 \sqrt{Q_{\text{in}}^2 + U_{\text{in}}^2} \cos(4\omega_{\text{hwp}}t - 4\phi_4 - \arctan \frac{U_{\text{in}}}{Q_{\text{in}}}), \quad (5)
 \end{aligned}$$

where,

$$\begin{aligned}
D_{0I} &= \frac{1}{2}M_{II} \\
D_{0Q} &= \frac{1}{4}(M_{QQ} + M_{UU}) \\
D_{0U} &= \frac{1}{4}(M_{QU} - M_{UQ}) \\
D_{2I} &= \frac{1}{2}\sqrt{M_{UI}^2 + M_{QI}^2} \\
\phi_0 &= \frac{1}{2}\arctan \frac{M_{UI}}{M_{QI}} \\
D_2 &= \frac{1}{2}\sqrt{M_{IQ}^2 + M_{IU}^2} \\
\phi_2 &= \frac{1}{2}\arctan \frac{M_{IU}}{M_{IQ}} \\
D_4 &= \frac{1}{4}\sqrt{(M_{QQ} - M_{UU})^2 + (M_{QU} + M_{UQ})^2} \\
\phi_4 &= \frac{1}{4}\arctan \frac{M_{QU} + M_{UQ}}{M_{QQ} - M_{UU}}.
\end{aligned}$$

From the demodulation at  $4\omega_{\text{hwp}}$ , we can extract the polarization power of the incident light. We define the modulation efficiency,  $\epsilon$ , to demonstrate the performance of the AHWP as:

$$\epsilon = \frac{D_4\sqrt{Q_{\text{in}}^2 + U_{\text{in}}^2}}{D_{0I}I_{\text{in}} + D_{0Q}Q_{\text{in}} + D_{0U}U_{\text{in}}}. \quad (6)$$

The modulation efficiency is the ratio between the signal power that is modulated at 4 times frequency of the HWP rotational frequency to the detected power. We also use  $\phi_4$  as the phase of the modulated signal to compare the calculation with the measured data. For an ideal single HWP,  $\Gamma$  becomes Eq. 9, we recover the following expression<sup>17</sup>

$$\epsilon = \frac{\sin^2 \frac{\delta}{2} \sqrt{Q_{\text{in}}^2 + U_{\text{in}}^2}}{I_{\text{in}} + \cos^2 \frac{\delta}{2} Q_{\text{in}}}. \quad (7)$$

In the case of  $(Q_{\text{in}}, U_{\text{in}}) = (0, 1)$ , the modulation efficiency is simply proportional to  $\sin^2 \frac{\delta}{2}$ .

In our development we aim for a modulation efficiency greater than 0.98 in a frequency range of 34-270 GHz with an incident angles up to 10 degrees for linearly-polarized incident light.

### 3 SAMPLE PREPARATION

#### 3.1 Design optimization

The AHWP consists of multiple sapphire plates with optic axes relatively rotated among the plates. We use sapphire as the birefringent material for the HWP. Sapphire has superior optical and thermal properties: about 10% difference in the refractive indices between the ordinary and the extraordinary rays,<sup>18</sup> the low loss-tangent at millimeter-wave frequency, and the high thermal conductivity,  $10^2$ - $10^3$  W/K/m, at a temperature of 4 - 10 K.<sup>19</sup>

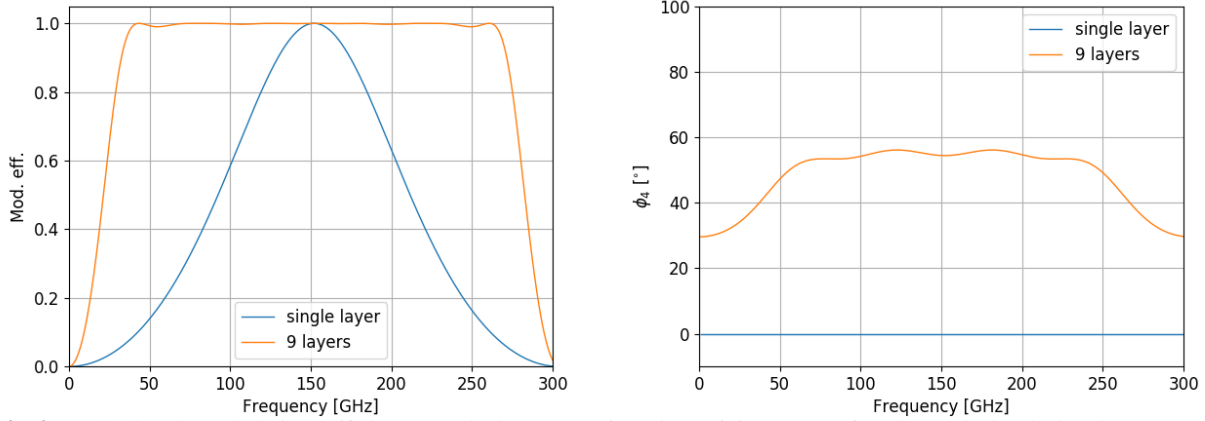


**Fig 2** Calculated modulation efficiency and phase as a function of frequency for the optimized nine-layer AHWP design. For comparison, we also show the calculated result of a single layer HWP. We calculate for  $S_{\text{in}} = (1, 1, 0, 0)$ .

We have conducted the design optimization for the AHWP using a simulation. The Mueller matrix of  $N$ -layer AHWP is described as

$$\Gamma_{\text{AHWP}} = \prod_i^N R(-\chi_i) \Gamma R(\chi_i), \quad (8)$$

where  $\Gamma$  is the Mueller matrix of a single birefringent plate,  $\chi_i$  is the orientation of the optic axis with respect to the  $x$ -axis. We assume that all plates of which the AHWP is composed have the same thickness  $d_c = \frac{1}{2} \frac{c}{\Delta n \nu_c}$ , and the same refractive indices, where  $\nu_c$  is the center of the frequency band and  $c$  is the speed of light. In this process, we did not consider any effects of reflection to save computational time. We verified the performance including the reflection after the completion of the optimization. Details of the calculation considering the effect of reflection are described in the appendix. Without any reflections, the Mueller matrix of a birefringent material is give in Eq. 9 with the retardance of  $\delta$ ,

$$\Gamma = \begin{pmatrix} 1 & 0 & 0 & 0 \\ 0 & 1 & 0 & 0 \\ 0 & 0 & \cos \delta & -\sin \delta \\ 0 & 0 & \sin \delta & \cos \delta \end{pmatrix}. \quad (9)$$

The design optimization is carried out by using a Monte-Carlo simulation written in Python. For the frequency range of 34 - 270 GHz, the center frequency is given as  $\nu_c = 152$  GHz, and the corresponding thickness is calculated to be 3.14 mm, where we use  $n_o = 3.047$  and  $n_e = 3.361$  for the refractive indices at low temperature<sup>18</sup> and we assume lossless sapphire plates. We vary the number of the HWP layers and the relative optic axis angles among the plates, and calculate  $I_{\text{out}}(t)$  for each frequency in the case of  $S_{\text{in}} = (1, 0, 1, 0)$ . We use the modulation efficiency  $\epsilon$  as the figure-of-merit for this optimization. As a result we have concluded that the nine-layer AHWP can cover almost all of the targeted bandwidth. Figure 2 shows the modulation efficiency and phase as a function of frequency with the optimized design for a single plate and the nine layers. Table 1 shows the optimized values of the relative angles in nine-layer AHWP.

number of plates	$d_c$ [mm]	$\chi_i$ [°]
9	3.14	0,18.5, 37.5, 73.9, 141.5, 73.9, 37.5, 18.5, 22.7

**Table 1** Designed values of the relative angles in the nine-layer AHWP. The thickness of each plate is identical.  $\chi_i$  is the optic axis angle of the  $i$ -th plate relative to the first layer.

### 3.2 Fabrication

We have fabricated the AHWP based on the optimized parameters. We use a commercially available sapphire sample, with a diameter of 100 mm. Although the optimized thickness is 3.14 mm for a targeted frequency range, we have used sapphire plates with a thickness of 2.53 mm, which was readily available. We believe that this slight difference in thickness is not critical for demonstration purposes. We measure the thickness of the sapphire along the circumference of the disk, and the variation of the thickness within the sample is found to be less than  $8 \mu\text{m}$ . The surface condition is unpolished. We have stacked the plates without glue at the interface of two plates, and fixed them with an aluminum holder as shown in Figure 3. The anti-reflection coating is not applied on any surfaces.

To stack the sapphire plates, we use the universal measurement machine (UMM). The UMM consists of a microscope and a rotating table. Each sapphire plate has an orientation flat (OF) at its side that is in perpendicular to the optic axis and can be used as the reference of the optic axis with the accuracy  $3^\circ$ . This accuracy is due to the uncertainty of a dicing capability in a sapphire manufacturing. Sapphire plates are stacked in the aluminum holder while adjusting with respect to OF to the designed orientation of the optic axis of each plate. Figure 3 shows the assembled nine-layer AHWP. Sapphire plates are fixed in the holder with pressure applied by an aluminum ring. The relative angular uncertainty between the OF of the plates is less than 10 arcmin.

After assembly, we evaluate the presence of air gaps between the layers. We investigate the thickness of the air gap by inserting several thin stainless steel plates with varying thickness ( $\geq 50 \mu\text{m}$ ), between layers of the AHWP. We identify that the air gap between the first and second layer is  $50 \mu\text{m}$ , and that air gaps between other layers are less than  $50 \mu\text{m}$ . We will account for the presence of the gap in the analysis.

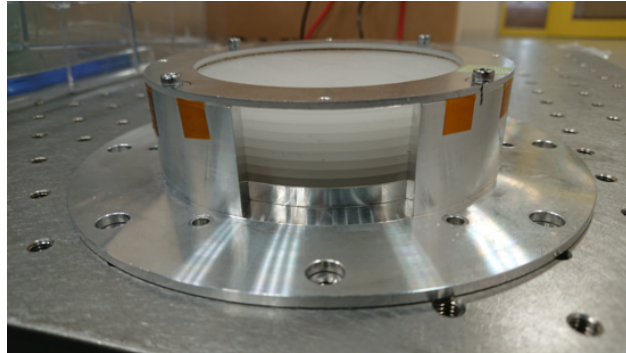


**Fig 3** The assembled nine-layer AHWP.

## 4 EXPERIMENT

### 4.1 Experimental setup

Figure 4 shows the setup for measuring the modulation efficiency and the transmittance in the frequency ranges of 33-140 GHz and 150-260 GHz. The millimeter waves are generated by a Continuous Wave (CW) generator and six different active multipliers. The CW generator can generate microwaves up to 20 GHz. Active multipliers up-convert the frequency of the signal from the CW generator. The multiple factors and bandwidths of individual active multipliers are  $\times 4$  (33-50 GHz),  $\times 4$  (50-75 GHz),  $\times 6$  (75-110 GHz),  $\times 8$  (90-140 GHz),  $\times 12$  (150-220 GHz) and  $\times 24$  (210-260 GHz). We pair the active multiplier with a diode detector for the measurements in each band. Two feedhorns for the source (the active multiplier) and for the detector are placed at the foci of the off-axis parabolic mirrors. The millimeter waves emitted from the source horn are collimated by the first mirror. The plane waves propagate through the first attenuator, the first wire grid, the 70 mm diameter aperture, the sample to measure, the second attenuator, and the second wire grid. The plane waves are focused by the second mirror to be fed to the detector horn. The millimeter wave from the source is linearly polarized. The detector used is a single polarization-sensitive detector. We use two wire grids to define the polarization angle of incident light to the sample. The signal is modulated by an optical chopper with a frequency of 80 Hz to be amplified by a lock-in amplifier. The detector outputs the detected power in voltage. We set the transmission axis of the two wire grids in parallel. All the measurements were performed at room temperature.

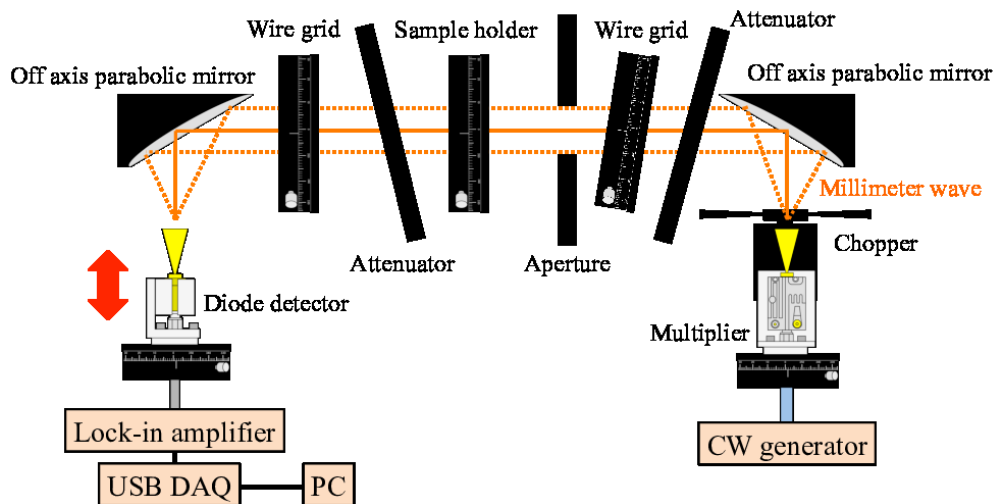


**Fig 4** A sketch of the measurement system. The millimeter waves propagate along the orange lines from the right hand to the left hand side of the figure. The aperture size is approx. 70 mm in diameter.

### 4.2 Measurement of refractive index

To predict the modulation efficiency, we need to know the two refractive indices of an a-cut sapphire plate at the room temperature. We obtain the indices by measuring transmittance, i.e. Fabry-Pérot interference, using the same setup in Figure 4. When the plane of polarization of the incident wave and the detector-sensitive direction are parallel to the optic axis, transmittance  $T$  and the

complex refractive index  $\tilde{n}$  of an extraordinary (ordinary) ray are simply related by Eq. 10 for the case of the normal incidence.<sup>20</sup> Since the loss tangent of sapphire is small enough to use the approximation,  $\tilde{n}$  is expressed using the refractive index  $n$  and the loss tangent  $\tan \delta$  in Eq. 11. The variable  $d$  is the thickness of the sapphire plate and  $k_0$  is the wave number in the vacuum,

$$T(\tilde{n}) = \left| \frac{2\tilde{n}}{2\tilde{n} \cos k_0 \tilde{n} d + i(\tilde{n}^2 + 1) \sin k_0 \tilde{n} d} \right|^2, \quad (10)$$

$$\tilde{n} \simeq n \left( 1 - \frac{i}{2} \tan \delta \right). \quad (11)$$

We measure the indices of one sapphire plate, and assume the same indices for the rest, which is valid because all the samples are originated from the same batch. We set the sapphire plate to the sample holder in Figure 4. We then measure output voltages of the lock-in amplifier at 33 to 140 GHz and 150 to 260 GHz in  $\sim 1$  GHz interval. After removing the a-cut sapphire plate, we remeasure output voltages of the lock-in amplifier for the same frequency range with the same frequency step. The spectral shape of transmittance for polarization parallel and perpendicular to the optic axis are computed by taking a ratio of the acquired data between the sapphire plate case and the air case.

### 4.3 Measurement of modulation efficiency

The nine-layer AHWP is mounted on a sample holder which can be automatically rotated by a stepping motor. The sample holder continuously rotates around the optical axis in this system with a revolution rate of  $\omega_{\text{hwp}} = 2\pi f_{\text{hwp}}$ , where  $f_{\text{hwp}}$  is about 0.02 Hz. The frequency of the electromagnetic source is swept during the rotation. We measure the modulated signal as the output voltage of the lock-in amplifier. The measured frequency range is 33 to 140 GHz and 150 to 260 GHz every 0.9 GHz. The measurement time at each frequency is 60 seconds, during which the AHWP rotates about 360 degrees. The sampling rate of the demodulated signal from the lock-in amplifier is 100 Hz. For each frequency, we fit the acquired data using Eq. 12.

$$I(t, \nu) = a_0(\nu) + \sum_{m=1}^8 a_m(\nu) \cos(m\omega_{\text{hwp}}t + m\phi_m(\nu)). \quad (12)$$

While acquiring data at all frequencies, the AHWP keeps on continuously rotating. The initial value of  $\phi_n$  is different for each frequency. This offset is recorded and subtracted for each  $\phi_n$  at given frequency. The  $m = 4$  component is the modulation signal of the AHWP. The  $m = 2$  component appears due to the difference of the frequency dependence of the transmittance between the two refractive indices in the HWP caused by the absence of anti-reflection coating. The other components are included to capture all the features even though we do not expect the odd  $m$  components within the framework of the formalism in this paper. We will address more on this point in the section 6. The modulation efficiency and the phase are obtained as  $a_4/a_0$  and  $\phi_4$ , respectively. The initial value of  $\phi_4$  is determined by the initial rotation angle of the sample holder. We have repeated the measurements for incident angles relative to the AHWP of 0 and  $\pm 10^\circ$  for  $p$ - and  $s$ -polarization, which corresponds to a typical field-of-view of the CMB telescope.

In many CMB experiments, the intensity of the observation signal is integrated by the detector with a specific bandwidth. Therefore, we introduce the band average modulation efficiency to

evaluate the integrated modulation signal. For the evaluation, we use the observation bandwidth of LiteBIRD below 270 GHz. We normalize  $I(t, \nu)$  by  $a_0$  for each frequency, and integrate this normalized modulated signals as

$$\int_{\nu_i}^{\nu_f} \frac{I(t, \nu)}{a_0(\nu)} d\nu = \sum_{\nu=\nu_i}^{\nu_f} \frac{I(t, \nu)}{a_0(\nu)} = A_0 + \sum_{m=1}^8 A_m \cos(m\omega_{\text{hwp}}t + m\phi_m), \quad (13)$$

where  $\nu_i$  and  $\nu_f$  are the lower and higher boundary in each frequency band, respectively. We define  $A_4/A_0$  as the band-averaged modulation efficiency.

## 5 RESULTS

### 5.1 Measurement of refractive index

From the fitting result for the frequency-dependent transmittance of the sapphire plate using Eq. 10 (Figure 5), we obtain the values of the refractive index and the loss tangent at room temperature for the a-cut sapphire plate, which are summarized in Table 2.

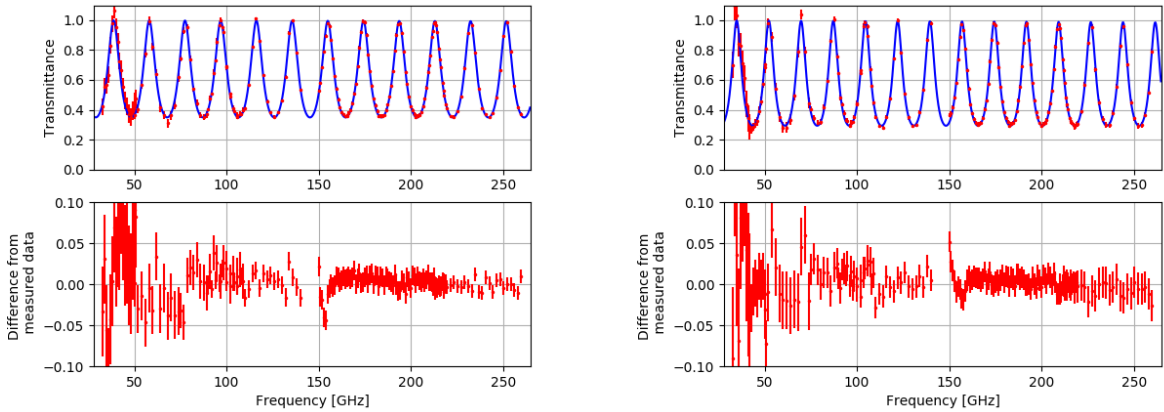


**Fig 5** The transmittance for the ordinary ray (left) and the extraordinary ray (right) for a a-cut sapphire plate. The top plot shows the measurement (the red dots with error-bars) and fitted (the blue solid line) results. The bottom plot shows the residuals of the fitting. The RMS of residuals is less than 3 %.

**Table 2** Fitted result to the refractive index and loss tangent for an a-cut sapphire plate at the room temperature.

Ordinary ray		Extraordinary ray	
Refractive index	Loss tangent ( $\times 10^{-4}$ )	Refractive index	Loss tangent ( $\times 10^{-4}$ )
$3.059 \pm 0.002$	$0.9 \pm 0.3$	$3.397 \pm 0.003$	$1.6 \pm 0.5$

### 5.2 Measurement of modulation efficiency

Figure 6 shows one example for the output voltages of the lock-in amplifier and fitted result using Eq. 12 as a function of the rotation angle at 150 GHz. For all frequencies and incident angles, we

confirm that the residual is less than 3% (in RMS) of the DC  $m = 0$  component. Figure 7 shows the frequency dependence of the modulation efficiency and the phase for each incident angle  $\theta$  with  $p$ - and  $s$ -polarization. The prediction for the normal incidence takes into account the reflections at plates and does not consider the air gaps between the plates. In the prediction, we use the values of  $n_o$  and  $n_e$  at the room temperature in Table 2. We can see two features in Figure 7: the sharp dips that appear at about every 18 GHz, and the fast oscillatory features that fluctuate quickly and with a small amplitude. The dips originate from Fabry-Pérot interference within each plate that composes the AHWP. By contrast, the oscillatory feature is from the reflection at the boundaries between the first/last plate and air.

Table 3 shows the measured band-averaged modulation efficiency and Table 4 shows the maximum difference of the phase variation within a bandwidth, which is defined as the LiteBIRD frequency band.

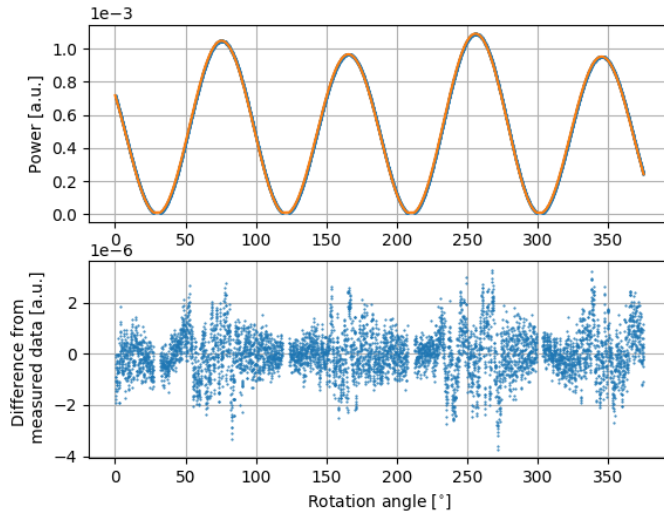


**Fig 6** The output voltages of the lock-in amplifier as a function of the HWP rotation angle at 150 GHz for the normal incident angle. The output voltage is proportional to the millimeter wave power injected into the detector. The top plot shows the measurement (the blue dots) and fitted (the orange solid line) results. The bottom plot shows the residuals of fitting.

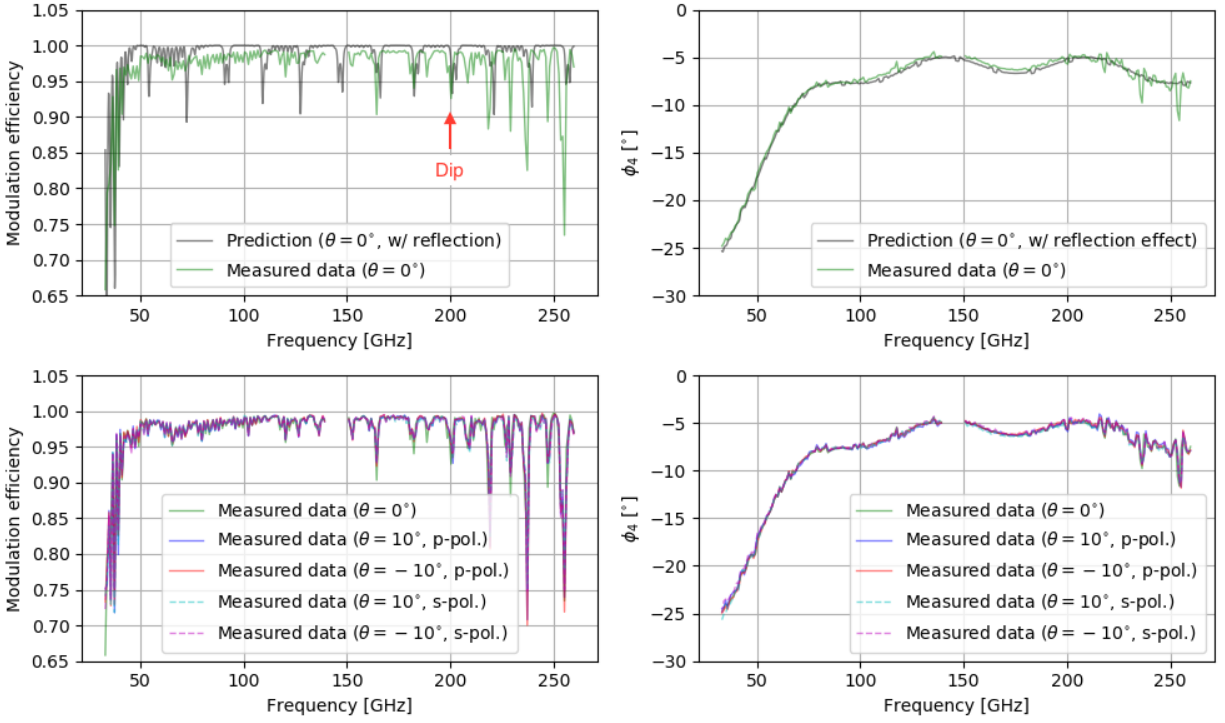


**Fig 7** The modulation efficiency and the phase from 33 to 260 GHz are plotted in every 0.9 GHz, where  $\theta$  is the incident angle of the millimeter waves for the AHWP. The predictions are plotted in every 0.2 GHz. The top side panels show the comparison of the measured data and the prediction for normal incidence. The bottom side panels show the comparison of normal and oblique incidence.

**Table 3** The measured band-averaged modulation efficiency within the bandwidth for the nine-layer AHWP at each incident angle.

		band-averaged modulation efficiency				
		$\theta = 0^\circ$	$\theta = 10^\circ$ (p-pol.)	$\theta = 10^\circ$ (s-pol.)	$\theta = -10^\circ$ (p-pol.)	$\theta = -10^\circ$ (s-pol.)
band [GHz]	bandwidth [%]					
40	30	0.902	0.895	0.892	0.897	0.900
50	30	0.961	0.960	0.959	0.961	0.960
60	23	0.971	0.970	0.970	0.970	0.971
68	23	0.969	0.969	0.969	0.969	0.970
78	23	0.976	0.975	0.976	0.976	0.977
89	23	0.981	0.981	0.981	0.982	0.982
100	23	0.985	0.985	0.986	0.985	0.986
119	30	0.984	0.983	0.983	0.983	0.984
140	30	0.984	0.984	0.984	0.984	0.984
166	30	0.983	0.984	0.983	0.984	0.983
195	30	0.979	0.979	0.978	0.979	0.979
235	30	0.959	0.955	0.955	0.954	0.954

**Table 4** The maximum difference of the phase variation within the bandwidth for the nine-layer AHWP at each incident angle.

		$\Delta\phi_4$				
		$\theta = 0^\circ$	$\theta = 10^\circ$ (p-pol.)	$\theta = 10^\circ$ (s-pol.)	$\theta = -10^\circ$ (p-pol.)	$\theta = -10^\circ$ (s-pol.)
band [GHz]	bandwidth [%]					
40	30	4.86°	5.11°	5.34°	5.05°	4.77°
50	30	6.86°	7.25°	6.78°	7.10°	6.64°
60	23	5.20°	5.41°	5.08°	5.56°	5.01°
68	23	3.90°	4.17°	3.82°	3.97°	3.86°
78	23	2.52°	2.86°	2.74°	2.65°	2.47°
89	23	0.82°	0.79°	0.68°	0.69°	0.74°
100	23	0.95°	0.94°	0.83°	0.89°	1.05°
119	30	3.15°	3.05°	3.25°	3.13°	3.22°
140	30	1.83°	1.83°	1.97°	1.86°	1.82°
166	30	1.49°	1.51°	1.41°	1.51°	1.74°
195	30	2.08°	2.31°	1.74°	1.98°	2.00°
235	30	7.12°	7.65°	6.63°	7.37°	6.84°

## 6 DISCUSSION

### 6.1 Sources of error

Figure 7 shows that the prediction and the measurement data are in good agreement for both modulation efficiency and phase. Nevertheless, we identify some discrepancies between the measurement results and the predictions. Here, we discuss possible sources of the the discrepancies between the measurement results and the predictions.

#### 6.1.1 Relative angular uncertainties

In the fabrication of the nine-layer stacked AHPW using the UMM, we find the relative angle position error of OF is less than 10 arcmin. The OF can be used as the reference of the optic axis with an accuracy of  $3^\circ$  (180 arcmin). Therefore the angular position uncertainty of the optic axis of the  $i$ -th plate is less than  $(i - 1) \times 190$  arcmin. Here we consider a conservative case; all the plates have angular position shifts of 190 arcmin relative to the former plate in the same direction. Figure 8 shows the comparison of the modulation efficiency and the phase with and without this angular position shifts. The bottom plot shows the difference between them. In this calculation, we ignore the air gaps and fix all the other parameters to their designed values. From the comparison result, the differences are found to be less than 0.33 (0.06 in RMS) for the modulation efficiency and less than  $17^\circ$  ( $14^\circ$  in RMS) for the phase.

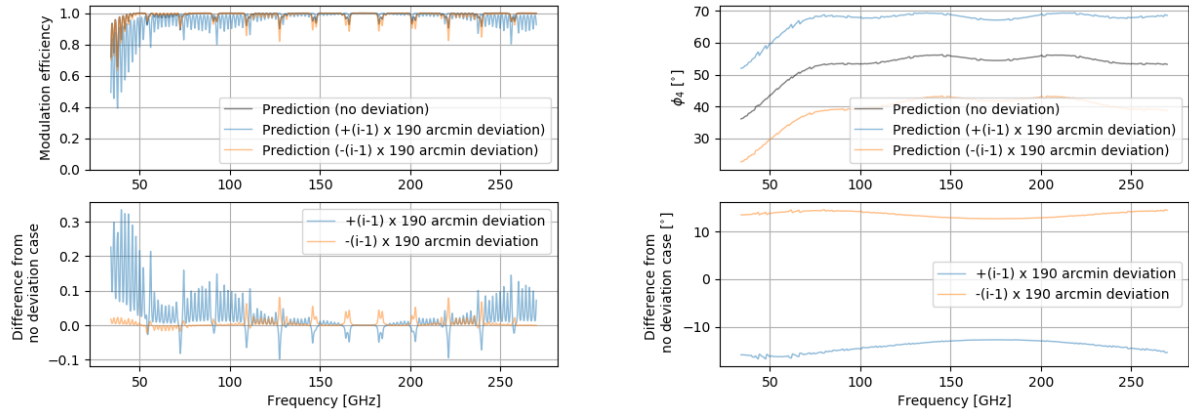


**Fig 8** Calculated results of the modulation efficiency and the phase for the nine-layer AHPW with and without the angular position shifts. The bottom plots show the differences from the case with no uncertainty.

#### 6.1.2 Thickness uncertainty of sapphire plates

We estimate the thickness uncertainty in individual sapphire plates to be  $\pm 4 \mu\text{m}$  from measurements of thickness variation along the circumference of the disk. We therefore calculate the modulation efficiency and the phase by assuming a plate thickness of 2.534 mm and 2.526 mm and compare it with the calculated result of the plate thickness of 2.530 mm. We again ignore the air gaps and set all the other parameters to designed values. From the comparison, the uncertainties of the modulation efficiency and the phase are estimated to be less than 0.05 (0.007 in RMS) and  $0.4^\circ$  ( $0.06^\circ$  in RMS), respectively.

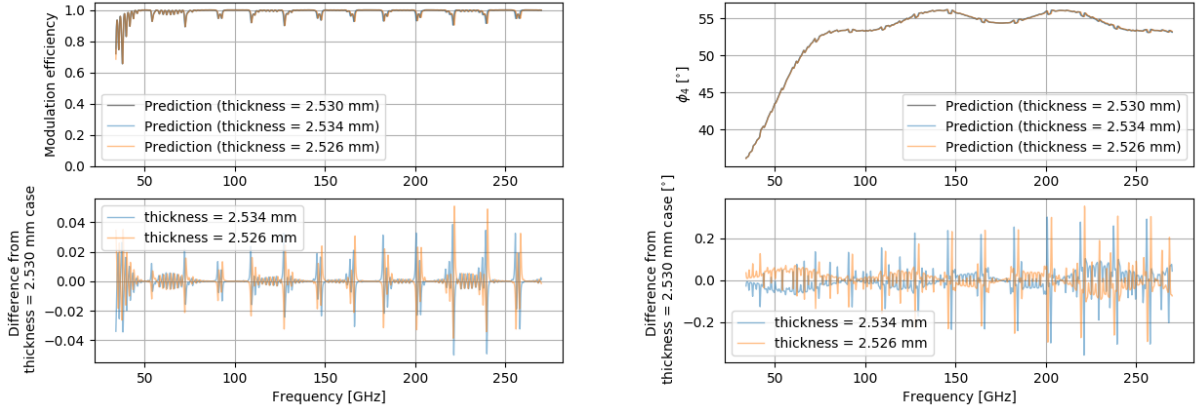


**Fig 9** Calculated results of the modulation efficiency and the phase of the nine-layer AHWP for the plate thicknesses of 2.530 mm, 2.534 mm and 2.526 mm. The bottom plot shows the differences of those values from the ones with 2.530 mm.

### 6.1.3 Refractive indices uncertainty

From Table 2, we estimate the difference between the two refractive indices of the a-cut sapphire to be  $\Delta n = 0.338 \pm 0.005$ . We compare the calculation results that  $\Delta n$  set to 0.343, 0.333 and 0.338. Here we ignore the air gaps and set all the other parameters to the designed values. With the comparison, we find the uncertainties in the modulation efficiency and phase to be 0.03 (0.003 in RMS) and  $0.4^\circ$  ( $0.2^\circ$  in RMS), respectively.

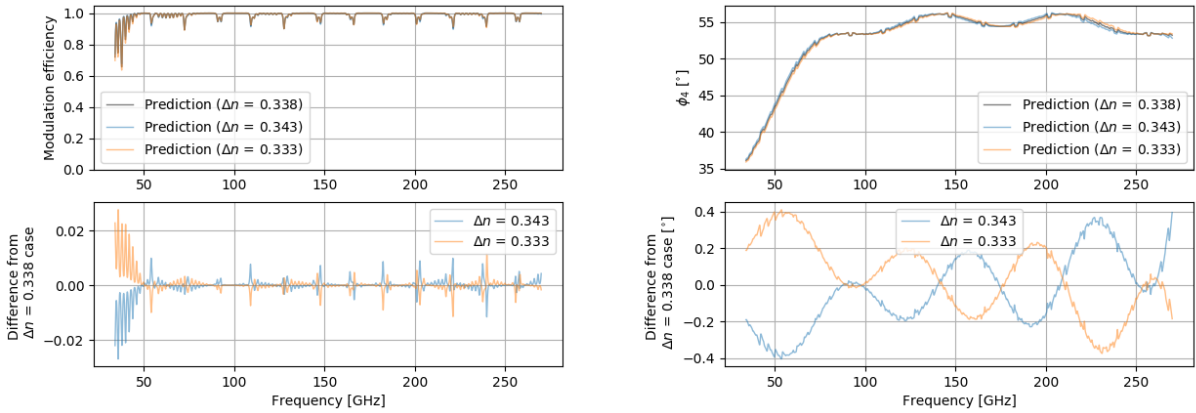


**Fig 10** Calculated results of the modulation efficiency and the phase of the nine-layer AHWP for the refractive index differences of 0.338, 0.343 and 0.333. The bottom plot shows the difference of them from the ones with 0.338.

### 6.1.4 The effect of air gaps

After the assembly of the AHWP, we identify the air gap between the first and second layer to be  $50 \mu\text{m}$ , and air gaps between other plates are found to be less than  $50 \mu\text{m}$ . We compare the modulation efficiency and the phase of the nine-layer AHWP in calculation with and without the  $10 \mu\text{m}$  and  $50 \mu\text{m}$  air gaps between all plates. Figure 11 shows the comparison results. We find no difference in the modulation efficiency and the phase around 175.3 GHz. This is because the

transmittance of all the sapphire plates is close to unity at this frequency and the air gaps do not contribute to the reflections at the boundaries of the plates. On the other hand, the influence of air gaps is large around the frequency where the dips and oscillatory feature in the modulation efficiency and the phase appear. This is because those two features originate from the reflections in the AHWP and the air gaps affect those reflections. For example, on the high frequency side, the depth of the dips and oscillatory feature monotonically increases according to the thickness of the air gap. On the low frequency side, where the thickness of the air gap is small, the dip depth is decreased, and where the thickness becomes large, it starts to increase. This trend is consistent with the difference between the prediction and the measured data in Figure 7. The air gaps cause the changes in the modulation efficiency and phase to be 0.9 in maximum (0.1 in RMS) and  $14^\circ$  at maximum ( $2^\circ$  in RMS), respectively. We find that the air gaps cause the most significant change in the AHWP performance for the modulation efficiency and the phase.

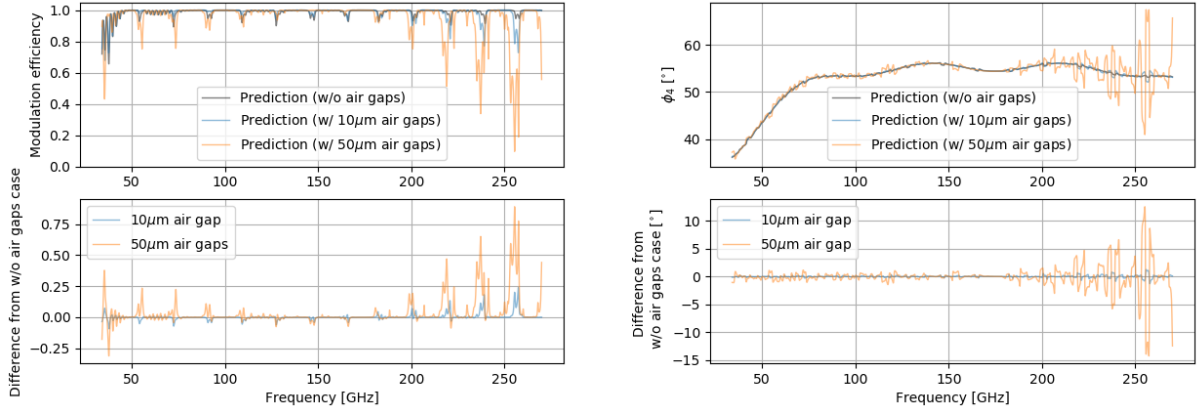


**Fig 11** Calculated results of the modulation efficiency and the phase with and without the air gaps for the nine-layer AHWP. The bottom plot shows the difference of them from the ones without the air gap.

### 6.1.5 Summary of sources of error

From the consideration in this subsection, we find that the air gaps is the largest source of the discrepancies between the measurements and the predictions. The second largest source is the relative angular uncertainty of the optic axis. The contributions of the uncertainties of the thickness and refractive indices are smaller than those of these two. Figure 12 shows a comparison of the measured data and the prediction that takes into account the largest source, air gaps. In Figure 12, the prediction and the measured data are in better agreement. In the prediction, the air gaps are inserted between each plate as a parallel flat plate having a refractive index of 1. The thickness of the air gap between the first and the second plate is set to  $50 \mu\text{m}$  and other gaps are set to  $8 \mu\text{m}$ . The thickness of the air gaps other than those between the first and second plates is obtained from the thickness variation along the circumference of the plates.

## 6.2 Amplitude of modulated signal for each mode

To obtain the modulation efficiency and the phase, we use Eq. 12 for the fitting of the modulated signal. Here, we discuss the components other than  $m = 4$ . The  $m = 2$  component appears due to

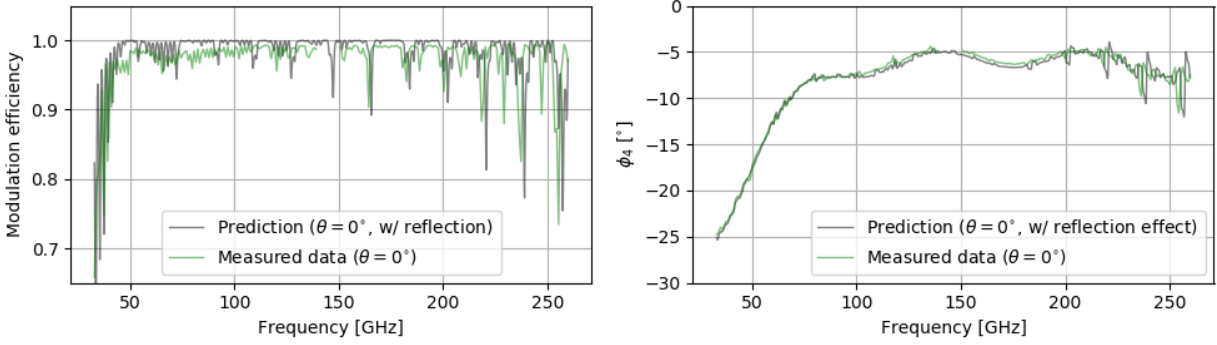


**Fig 12** The modulation efficiency and the phase from 33 to 260 GHz are plotted every 0.9 GHz. The predictions takes into account the air gaps and are plotted every 0.2 GHz.

the difference of the frequency-dependent transmittance between the two refractive indices in the HWP caused by the absence of the anti-reflection coating. Figure 13 shows a comparison of the measured data and the prediction of the  $m = 2$  component which takes into account the air gaps. While we think the model of the air gap is not complete, we qualitatively recover the agreement between the prediction and the measured data.

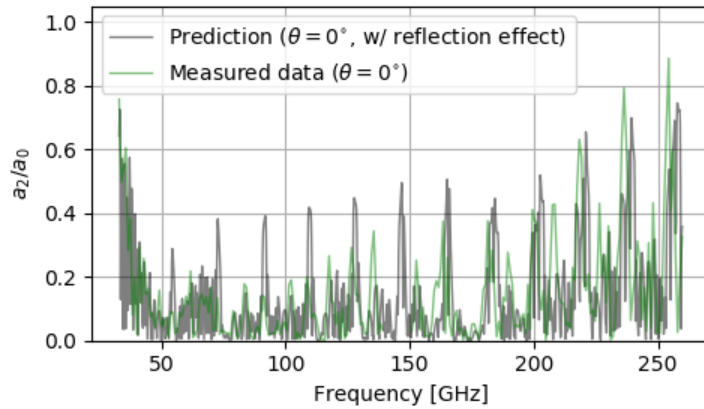


**Fig 13** The amplitude of  $m = 2$  component from 33 to 260 GHz are plotted every 0.9 GHz. The predictions takes into account the air gaps and are plotted every 0.2 GHz.

The origin of other modes,  $m = 1, 3, 5, 6, 7, 8$ , is not physically motivated within the formalism described in Eq. 5. The peak amplitude is generally signal-to-noise above 100 for  $m = 1, 3, 5, 6, 8$  in the range of above 40 GHz. Thus, the identified peaks are not due to the noise. One of the potential contributors to the peaks at  $m \neq 2, 4$  is from the imperfection of the assembly. Figure 14 shows the measured amplitude of the mode at  $m = 1, 3, 5, 6, 7, 8$ . For the mode  $m = 1, 3, 5$ , we identify the general trend of higher amplitude as it extends to the higher frequency. This is generally consistent with the effect of the air gap. The modes at  $m = 6, 7, 8$ , on the other hand, show the different tendency.

We also looked at the correlation between  $m = 1$  and  $m = 3, 5$  as shown in Figure 15. If the majority of the effect is due to the air gap and the air gap has a wedge-like shape, we expect

the rotational synchronous  $m = 1$  mode and potentially higher harmonics. Figure 15 shows the positive correlation between the  $m = 1$  mode and the  $m = 3, 5$ , which supports the idea of the effect of the wedge shape air gap and its harmonics.

The  $m \neq 4$  modes can be filtered out at the demodulation step. Thus, we decide not to explore beyond the identification of the existence of  $m \neq 4$  mode.

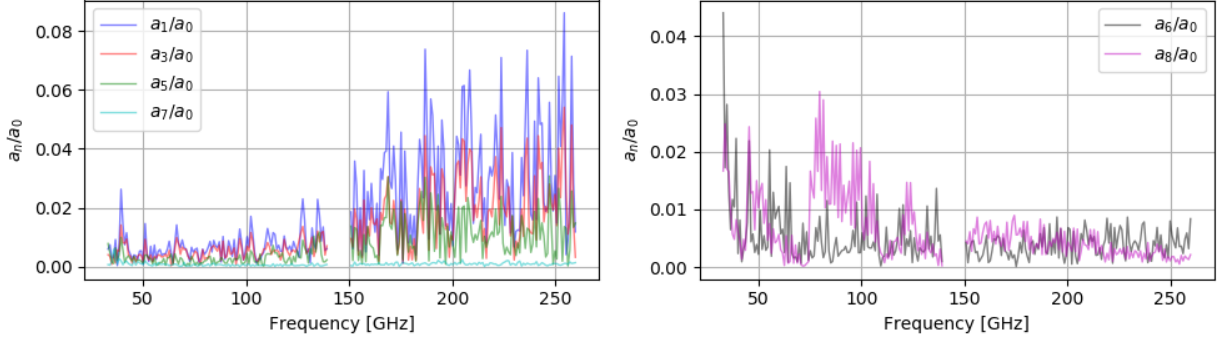


**Fig 14** The  $m = 1, 3, 5, 6, 7, 8$  components from 33 to 260 GHz are plotted in every 0.9 GHz.

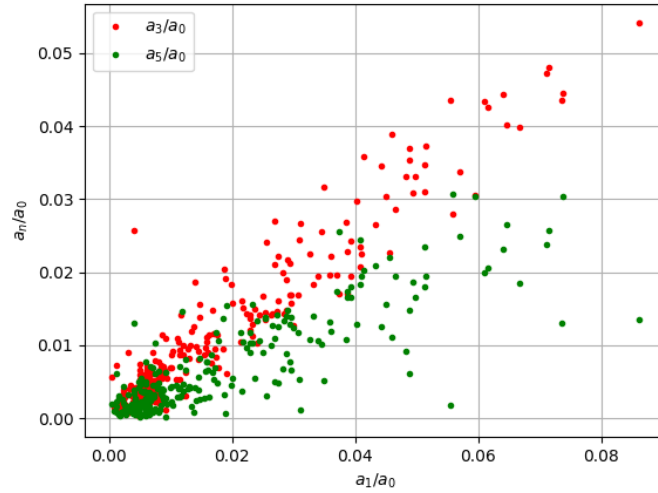


**Fig 15** The correlation of  $a_1/a_0$  and  $a_3/a_0, a_5/a_0$  from 33 to 260 GHz. The data is every 0.9 GHz.

### 6.3 Dependency for incident angle

In Table 3 we show the band-averaged modulation efficiencies with the incident angle of 10 degrees. The differences of the efficiencies between normal and the 10 degree oblique incidence are less than 0.005 (0.01) for the highest (lowest) bands. For the other bands, the differences are less than 0.001. The bottom side panels of Figure 7 show the modulation efficiency and the phase for the two incident angles, suggesting there is no significant difference between them.

In order to understand the incident angle dependence more precisely, we repeat the measurement with a finer frequency step of 0.15 GHz between 230 and 240 GHz, and with incident angle of  $\pm 5^\circ$ . Figure 16 shows the incident angle dependencies, and we find that there is a frequency shift of the dip. In case of the incident angle of  $5^\circ$  ( $10^\circ$ ), the refraction angle at the first plate of the AHWP is calculated to be about  $1.5^\circ$  ( $3^\circ$ ) for each ray. Since the difference in the refractive indices is small at the boundary between the two sapphire plates, the refraction angles within each plate are similar to the first plate. When  $\theta \neq 0$ , frequencies of Fabry-Pérot interference spectrum scaled by  $(\cos \theta)^{-1}$  compared with the normal incidence ( $\theta = 0$ ). That causes the frequency shift to the higher side. For the refraction angle of  $1.5^\circ$  ( $3^\circ$ ), the frequency shift is computed to be about 0.08 (0.33) GHz. The estimation of the frequency shift is in good agreement to the shift measured in the modulation efficiency and the phase. Therefore, we find the observed frequency shift can be explained by the incident angle dependence.

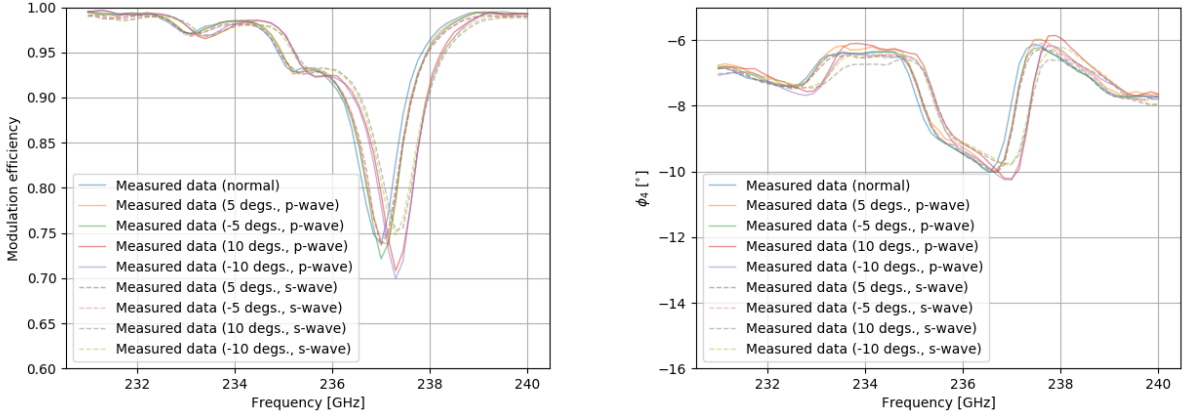


**Fig 16** Frequency dependence of the modulation efficiency and the phase for 230 to 240 GHz. The data points of the measurement result are plotted for every 0.15 GHz.

#### 6.4 Further design optimization

In spite of the fact that the nine layer AHWP becomes broadband as expected, the band-averaged modulation efficiency is lower than 0.98 in some bands. We find three reasons why the band averaged modulation efficiency is lower than 0.98. The first two reasons are due to the hardware preparation, and the third one arises from the AHWP design. The first reason is the fact that the thickness of the sapphire plates used is slightly thinner than the optimized one (Table 1). This causes an overall frequency shift to higher frequency of the modulation efficiency, dropping the efficiency at the lower frequency bands. The second reason is caused by the large dips and oscillatory features caused by the air gaps, which also decreases the overall modulation efficiency when averaged over the band. Particularly, this influence is large on the higher frequency bands. The third reason is caused by the large phase variation on the higher and lower frequency bands (Table 4). Table 5 shows the prediction of the averaged modulation efficiencies and the maximum phase variation with reflection effects, no air gaps and the optimized thickness. The band averaged modulation efficiencies at the highest and lower frequency band are less than 0.98. This exception is due to the large phase variation in the frequency band. The phase variation decreases in the amplitude of the modulated signal that is integrated in the band and the band averaged modulation

efficiency. Therefore the averaged value gets smaller, indicating that the phase variation is important. Therefore, we study the further design optimization that minimizes the phase variation within the band while the modulation efficiency is kept high enough in preparation.

**Table 5** The prediction of the averaged modulation efficiency and the maximum phase variation of the nine-layer AHWP with reflection effects, no air gaps, and optimized thickness.

band [GHz]	bandwidth [%]	band averaged modulation efficiency	$\Delta\phi_4$
40	30	0.969	6.26°
50	30	0.977	7.49°
60	23	0.982	3.87°
68	23	0.991	2.07°
78	23	0.995	0.55°
89	23	0.995	0.85°
100	23	0.989	2.41°
119	30	0.990	1.87°
140	30	0.993	1.98°
166	30	0.993	2.01°
195	30	0.990	3.08°
235	30	0.938	16.46°

## 7 CONCLUSIONS

We design and evaluate the prototype of the nine-layer AHWP for use in CMB experiments. We find the measurements in the modulation efficiency and the phase at the room temperature are in good agreement with the predictions. Thus, we demonstrate our nine-layer AHWP to be broadband. However, we find small discrepancies between the measurements and the predictions. The primary contribution is attributed to the existence of air gaps between the stacked plates. The uncertainty in the relative angular position among the plates is the second contribution. We find the uncertainties in the plate thickness and refractive indices are negligible. The agreement gets even better when those effects are considered.

We measure the incident angle dependence of the modulation efficiency and the phase in the incident angle range comparable to the field of view of typical CMB observations, about 10 degrees. The dependence of the incident angle is found to be explained by the internal reflections in individual plates.

In many CMB experiments, the intensity of the observation signal is integrated by the detector in a specific bandwidth. Therefore, we average the modulation efficiency over the bandwidth to obtain the value usable for the experiments. From the evaluation using the band-averaged modulation efficiency, we find that the smaller the phase variation in the bandwidth, the larger the averaged modulation efficiency. Therefore, the optimization to obtain higher modulation efficiency requires us to have uniform phase values in the bandwidth, which will be presented in future work.

## Acknowledgments

This work is supported by JSPS KAKENHI Grant Number JP17H01125, JP15H05441, JP15H05891, JP17K14272, JP18J20148 and JSPS Core-to-Core Program, A. Advanced Research Networks, and the World Premier International Research Center Initiative (WPI Initiative), MEXT, Japan. We would like to thank Dr. Samantha Stever for editorial suggestions to this paper.

## APPENDIX

### Prediction of the modulation efficiency containing the effect of reflection

In order to predict the modulation efficiency and the phase for the AHWP which does not have the anti-reflection structure in its surface, we calculate a  $4 \times 4$  matrix  $t(\chi)$  which transfers a vector consisting of the electromagnetic field  $(E_x, H_y, E_y, -H_x)$  between the two surfaces of a single birefringent material plate, where  $E_x$  ( $H_x$ ) and  $E_y$  ( $H_y$ ) are the electric (magnetic) field amplitude along the  $x$ - and  $y$ -axis, respectively. For this calculation, we refer to Thomas Essinger-Hileman (2014) as a reference.<sup>21</sup> We denote a value of  $\chi$  as the angle of the optic axis with respect to the  $x$  axis,  $d$  as the thickness of the plate,  $n_o$  and  $n_e$  are refractive indices of the extraordinary and the ordinary rays, respectively, and  $\delta_o = k_0 n_o d$  and  $\delta_e = k_0 n_e d$  as the retardance of the electric fields along each ray,  $\epsilon_0$  and  $\mu_0$  as the dielectric constant and the magnetic permeability in vacuum. In Eq. 14, we give the calculation results of  $t(\chi)$  for the normal incidence for a single wave plate.

$$t(\chi) = \begin{pmatrix} \sin^2 \chi \cos \delta_o + \cos^2 \chi \cos \delta_e & \frac{\sin^2 \chi n_e \sin \delta_o + \cos^2 \chi n_o \sin \delta_e}{n_o n_e C} & \cos \chi \sin \chi (\cos \delta_e - \cos \delta_o) & \frac{\cos \chi \sin \chi (n_o \sin \delta_e - n_e \sin \delta_o)}{n_o n_e C} \\ C(\sin^2 \chi n_o \sin \delta_o + \cos^2 \chi n_e \sin \delta_e) & \sin^2 \chi \cos \delta_o + \cos^2 \chi \cos \delta_e & C \cos \chi \sin \chi (n_e \sin \delta_e - n_o \sin \delta_o) & \frac{\cos \chi \sin \chi (\cos \delta_e - \cos \delta_o)}{\cos^2 \chi n_e \sin \delta_o + \sin^2 \chi n_o \sin \delta_e} \\ \cos \chi \sin \chi (\cos \delta_e - \cos \delta_o) & \frac{\cos \chi \sin \chi (n_o \sin \delta_e - n_e \sin \delta_o)}{n_e n_o C} & \cos^2 \chi \cos \delta_o + \sin^2 \chi \cos \delta_e & \frac{n_e n_o C}{\sin^2 \chi \cos \delta_e + \cos^2 \chi \cos \delta_o} \\ C \cos \chi \sin \chi (n_e \sin \delta_e - n_o \sin \delta_o) & \cos \chi \sin \chi (\cos \delta_e - \cos \delta_o) & C(\cos^2 \chi n_o \sin \delta_o + \sin^2 \chi n_e \sin \delta_e) & \sin^2 \chi \cos \delta_e + \cos^2 \chi \cos \delta_o \end{pmatrix} \quad (14)$$

$$C = \sqrt{\frac{\epsilon_0}{\mu_0}} \quad (15)$$

The transfer matrix  $T$  for a  $N$ -layer AHWP is calculated by multiplying the matrices  $t(\chi_i)$ , where  $\chi_i$  is the optic axis orientation in  $i$ -the layer:

$$T = \prod_i^N t(\chi_i). \quad (16)$$

Using  $T$ , we obtain a Jones matrix of the  $N$ -layer AHWP as Eq. 17.

$$J = \begin{pmatrix} J_{00} & J_{01} \\ J_{10} & J_{11} \end{pmatrix} = 2a_8 \begin{pmatrix} a_5 + a_7 & -a_1 - a_3 \\ -a_4 - a_6 & a_0 + a_2 \end{pmatrix} \quad (17)$$

$$\begin{aligned}
a_0 &= T_{00} + T_{01}C \\
a_1 &= T_{02} + T_{03}C \\
a_2 &= \frac{T_{10}}{C} + T_{11} \\
a_3 &= \frac{T_{12}}{C} + T_{13} \\
a_4 &= T_{20} + T_{21}C \\
a_5 &= T_{22} + T_{23}C \\
a_6 &= \frac{T_{30}}{C} + T_{31} \\
a_7 &= \frac{T_{32}}{C} + T_{33} \\
a_8 &= \frac{1}{(a_0 + a_2)(a_5 + a_7) - (a_1 + a_3)(a_4 + a_6)}
\end{aligned}$$

Using Eq. 17, we obtain the relation of electric fields before and after passing through the  $N$ -layer AHWP as a function of the rotation angle  $\rho$ :

$$\begin{pmatrix} E_{out}^x \\ E_{out}^y \end{pmatrix} = \begin{pmatrix} \cos \rho & \sin \rho \\ -\sin \rho & \cos \rho \end{pmatrix} J \begin{pmatrix} \cos \rho & -\sin \rho \\ \sin \rho & \cos \rho \end{pmatrix} \begin{pmatrix} E_{in}^x \\ E_{in}^y \end{pmatrix}, \quad (18)$$

where  $(E_{in}^x, E_{in}^y)$  and  $(E_{out}^x, E_{out}^y)$  are electric fields of the incoming and outgoing light. For our measurements,  $(E_{in}^x, E_{in}^y) = (1, 0)$  and we measured the value of the intensity of the electric field:  $I(\rho) = |E_{out}^x|^2$ . The predictions of the modulation efficiency and the phase of modulated signal containing the effect of reflection are obtained to be  $A_4/A_0$  and  $\phi_4$  with following relations.

$$I(\rho) = |E_{out}^x|^2 = A_0 + A_2 \cos\{2(\rho + \phi_2)\} + A_4 \cos\{4(\rho + \phi_4)\} \quad (19)$$

$$\begin{aligned}
\alpha_1 &= \frac{J_{11}\bar{J}_{11} + J_{00}\bar{J}_{00} - J_{00}\bar{J}_{11} - J_{11}\bar{J}_{00} - J_{10}\bar{J}_{10} - J_{01}\bar{J}_{10} - J_{10}\bar{J}_{01} - J_{01}\bar{J}_{01}}{8} \\
\alpha_2 &= \frac{-J_{10}\bar{J}_{11} - J_{01}\bar{J}_{11} - J_{11}\bar{J}_{10} - J_{11}\bar{J}_{01} + J_{00}\bar{J}_{10} + J_{10}\bar{J}_{00} + J_{00}\bar{J}_{01} + J_{01}\bar{J}_{00}}{8} \\
\beta_1 &= \frac{J_{00}\bar{J}_{00} - J_{11}\bar{J}_{11}}{2} \\
\beta_2 &= \frac{J_{10}\bar{J}_{11} + J_{01}\bar{J}_{11} + J_{11}\bar{J}_{10} + J_{11}\bar{J}_{01} + J_{00}\bar{J}_{10} + J_{10}\bar{J}_{00} + J_{00}\bar{J}_{01} + J_{01}\bar{J}_{00}}{4}
\end{aligned}$$

$$\begin{aligned}
A_0 &= \frac{3J_{11}\bar{J}_{11} + 3J_{00}\bar{J}_{00} + J_{00}\bar{J}_{11} + J_{11}\bar{J}_{00} + J_{10}\bar{J}_{10} + J_{01}\bar{J}_{10} + J_{10}\bar{J}_{01} + J_{01}\bar{J}_{01}}{8} \\
A_2 &= \sqrt{\beta_1^2 + \beta_2^2} \\
A_4 &= \sqrt{\alpha_1^2 + \alpha_2^2} \\
\phi_2 &= \begin{cases} \frac{\arctan(\beta_2/\beta_1)}{2} & (\beta_1 > 0) \\ \frac{\arctan(\beta_2/\beta_1)+\pi}{2} & (\beta_1 < 0) \end{cases} \\
\phi_4 &= \begin{cases} \frac{\arctan(\alpha_2/\alpha_1)}{4} & (\alpha_1 > 0) \\ \frac{\arctan(\alpha_2/\alpha_1)+\pi}{4} & (\alpha_1 < 0) \end{cases}
\end{aligned}$$

### References

- 1 Wu *et al.*, “Maxipol: data analysis and results,” *The Astrophysical Journal* **665**, 55 (2007).
- 2 A. Kusaka *et al.*, “Modulation of cosmic microwave background polarization with a warm rapidly rotating half-wave plate on the atacama b-mode search instrument,” *Review of Scientific Instruments* **85**(024501) (2014).
- 3 B. Reichborn-Kjennerud *et al.*, “Ebex: a balloon-borne cmb polarization experiment,” *Proc. SPIE* **7741**(77411C) (2010).
- 4 T. E. Montory *et al.*, “Spider: a new balloon-borne experiment to measure cmb polarization on large angular scales,” *Proc. SPIE* **6267**(62670R) (2006).
- 5 P. Collaboration, “A measurement of the cosmic microwave background b-mode polarization power spectrum at sub-degree scales with polarbear,” *Astrophysical Journal* **794**, 171 (2014).
- 6 Y. Sakurai *et al.*, “Design and development of a polarization modulator unit based on a continuous rotating half-wave plate for litebird,” in *Millimeter, Submillimeter, and Far-Infrared Detectors and Instrumentation for Astronomy IX, Proc. SPIE* **10708**(107080E) (2018).
- 7 C. A. Hill *et al.*, “Design and development of an ambient-temperature continuously-rotating achromatic half-wave plate for cmb polarization modulation on the polarbear-2 experiment,” in *Millimeter, Submillimeter, and Far-Infrared Detectors and Instrumentation for Astronomy VIII, Proc. SPIE* **9914**(99142U) (2016).
- 8 N. Galitzki *et al.*, “The simons observatory: instrument overview,” in *Millimeter, Submillimeter, and Far-Infrared Detectors and Instrumentation for Astronomy IX, Proc. SPIE* **10708**(1070804) (2018).
- 9 F. Columbro *et al.*, “The short wavelength instrument for the polarization explorer balloon-borne experiment: Polarization modulation issues,” *Astronomische Nachrichten* **340**, 83–88 (2019).
- 10 S. Pancharatnam, “Achromatic combinations of birefringent plates part i. an achromatic circular polarizer,” *Raman Research Institute, Bangalore, Memoir* **71**, 130–136 (1955).
- 11 S. Pancharatnam, “Achromatic combinations of birefringent plates part ii. an achromatic quarter-wave plate,” *Raman Research Institute, Bangalore, Memoir* **71**, 137–144 (1955).
- 12 S. Hanany *et al.*, “Millimeter-wave achromatic half-wave plate,” *Applied Optics* **44**, 4666–4670 (2005).

- 13 G. Savini *et al.*, “Achromatic half-wave plate for submillimeter instruments in cosmic microwave background astronomy: modeling and simulation,” *Applied Optics* **45**, 8907–8915 (2006).
- 14 G. Pisano *et al.*, “Achromatic half-wave plate for submillimeter instruments in cosmic microwave background astronomy: experimental characterization,” *Applied Optics* **45**, 6982–6989 (2006).
- 15 H. Ishino *et al.*, “Litebird, lite satellite for the study of b-mode polarization and inflation from cosmic microwave background radiation detection,” in *Space Telescopes and Instrumentation 2016: Optical, Infrared, and Millimeter Wave, Proc. SPIE* **9904**(99040X) (2016). [doi: 10.1117/12.2231995].
- 16 K. Komatsu *et al.*, “Prototype design and evaluation of the nine-layer achromatic half-wave plate for the litebird low frequency telescope,” in *Millimeter, Submillimeter, and Far-Infrared Detectors and Instrumentation for Astronomy IX, Proc. SPIE* **10708**(1070847) (2018).
- 17 T. Matsumura *et al.*, “Analysis of performance of three- and five-stack achromatic half-wave plates at millimeter wavelengths,” *Applied Optics* **48**, 3614–3625 (2009).
- 18 B. R. Johnson, *MAXIPOL: A Bolometric, Balloon-Borne Experiment for Measuring the Polarization Anisotropy of the Cosmic Microwave Background Radiation*. Ph.d. thesis, University of Minnesota, Twin Cities (2004).
- 19 F. Pobell, *Matter and Methods at Low Temperatures*(Third Edition), Springer (2007).
- 20 E. Hecht, *Optics II*, Addison-Wesley (1998).
- 21 T. Essinger-Hileman, “Transfer matrix for treating stratified media including birefringent crystals,” *Applied Optics* **53**, 4264–4265 (2014).

**First Author** is a PhD student at Okayama University. He received his BS and MS degrees in physics from Okayama University in 2016 and 2018, respectively. His current research interests the verification of inflation theory using B-mode polarization of CMB created by the primordial gravitational waves. Related to it, he is developing the polarization modulator of LiteBIRD.

Biographies and photographs of the other authors are not available.

## List of Figures

- 1 A conceptual sketch of the three-layer AHWP polarimetry. The linearly polarized plane waves propagate from left to right in this figure. An example of the modulated signal resulting from one revolution of the HWP is shown in the most right hand side. The amplitude is related to the polarized intensity and the phase is related to the polarization angle of the incident radiation.
- 2 Calculated modulation efficiency and phase as a function of frequency for the optimized nine-layer AHWP design. For comparison, we also show the calculated result of a single layer HWP. We calculate for  $S_{\text{in}} = (1, 1, 0, 0)$ .
- 3 The assembled nine-layer AHWP.
- 4 A sketch of the measurement system. The millimeter waves propagate along the orange lines from the right hand to the left hand side of the figure. The aperture size is approx. 70 mm in diameter.

- 5 The transmittance for the ordinary ray (left) and the extraordinary ray (right) for a a-cut sapphire plate. The top plot shows the measurement (the red dots with error-bars) and fitted (the blue solid line) results. The bottom plot shows the residuals of the fitting. The RMS of residuals is less than 3 %.
- 6 The output voltages of the lock-in amplifier as a function of the HWP rotation angle at 150 GHz for the normal incident angle. The output voltage is proportional to the millimeter wave power injected into the detector. The top plot shows the measurement (the blue dots) and fitted (the orange solid line) results. The bottom plot shows the residuals of fitting.
- 7 The modulation efficiency and the phase from 33 to 260 GHz are plotted in every 0.9 GHz, where  $\theta$  is the incident angle of the millimeter waves for the AHWP. The predictions are plotted in every 0.2 GHz. The top side panels show the comparison of the measured data and the prediction for normal incidence. The bottom side panels show the comparison of normal and oblique incidence.
- 8 Calculated results of the modulation efficiency and the phase for the nine-layer AHWP with and without the angular position shifts. The bottom plots show the differences from the case with no uncertainty.
- 9 Calculated results of the modulation efficiency and the phase of the nine-layer AHWP for the plate thicknesses of 2.530 mm, 2.534 mm and 2.526 mm. The bottom plot shows the differences of those values from the ones with 2.530 mm.
- 10 Calculated results of the modulation efficiency and the phase of the nine-layer AHWP for the refractive index differences of 0.338, 0.343 and 0.333. The bottom plot shows the difference of them from the ones with 0.338.
- 11 Calculated results of the modulation efficiency and the phase with and without the air gaps for the nine-layer AHWP. The bottom plot shows the difference of them from the ones without the air gap.
- 12 The modulation efficiency and the phase from 33 to 260 GHz are plotted every 0.9 GHz. The predictions takes into account the air gaps and are plotted every 0.2 GHz.
- 13 The amplitude of  $m = 2$  component from 33 to 260 GHz are plotted every 0.9 GHz. The predictions takes into account the air gaps and are plotted every 0.2 GHz.
- 14 The  $m = 1, 3, 5, 6, 7, 8$  components from 33 to 260 GHz are plotted in every 0.9 GHz.
- 15 The correlation of  $a_1/a_0$  and  $a_3/a_0$ ,  $a_5/a_0$  from 33 to 260 GHz. The data is every 0.9 GHz.
- 16 Frequency dependence of the modulation efficiency and the phase for 230 to 240 GHz. The data points of the measurement result are plotted for every 0.15 GHz.

## List of Tables

- 1 Designed values of the relative angles in the nine-layer AHWP. The thickness of each plate is identical.  $\chi_i$  is the optic axis angle of the  $i$ -th plate relative to the first layer.

- 2 Fitted result to the refractive index and loss tangent for an a-cut sapphire plate at the room temperature.
- 3 The measured band-averaged modulation efficiency within the bandwidth for the nine-layer AHWP at each incident angle.
- 4 The maximum difference of the phase variation within the bandwidth for the nine-layer AHWP at each incident angle.
- 5 The prediction of the averaged modulation efficiency and the maximum phase variation of the nine-layer AHWP with reflection effects, no air gaps, and optimized thickness.